Supramolecular Control of Photoinduced Electron Transfer between Tungsten Halide Clusters and Polyoxometalates in Water

Thi Huyen My Dang, Anam Fatima, Maxime Lajoye, Clément Falaise, Emmanuel Cadot, Adèle Renaud, Serge Paofai, Rachel Méallet, Céline Dablemont, Karine Steenkeste, et al.

Supramolecular control of photoinduced electron transfer between tungsten halide clusters and polyoxometalates in water

*Thi Huyen My Dang,[a] Anam Fatima,[a] Maxime Lajoye,[b] Clément Falaise,[b] Emmanuel Cadot,[b] Adèle Renaud,[c] Serge Paofai,[c] Rachel Meallet,[a] Céline Dablemont,[a] Karine Steenkeste,[a] Stéphane Cordier,[*c] Mohamed Haouas,[*b] Thomas Pino,[*a] Minh-Huong Ha-Thi[*a]*

[a] Université Paris-Saclay, CNRS, Institut des Sciences Moléculaires d'Orsay (ISMO), 91405 Orsay, France.

Email : thomas.pino@universite-paris-saclay.fr; minh-huong.ha-thi@universite-paris-saclay.fr

[b] Université de Versailles Saint-Quentin-en-Yvelines, CNRS, Institut Lavoisier de Versailles (ILV), 78035, Versailles Cedex, France.

Email : mohamed.haouas@uvsq.fr

[c] Université de Rennes, CNRS, Institut des Sciences Chimiques de Rennes (ISCR), 35000 Rennes, France.

Email : stephane.cordier@univ-rennes.fr

ABSTRACT. Identifying systems composed of earth-abundant elements capable of photoinduced electron-transfer represents a major breakthrough for the development of sustainable photocatalytic

processes. Herein, we demonstrate that octahedral tungsten-halide clusters constitute a promising new class of robust photosensitizers, owing to their exceptional chemical stability, intense luminescence, and long-lived triplet excited states. Upon irradiation in aqueous solution, these species transfer an electron to polyoxometalates (POMs), well-known molecular catalysts capable of multi-electron redox chemistry. More specifically, we investigate the photophysical properties of supramolecular systems combining the cluster-based motif $[\{W_6I^i_8\}Cl^a_6]^{2-}$ and a series of archetypal POMs ($[PW_{12}O_{40}]^{3-}$, $[SiW_{12}O_{40}]^{4-}$, $[BW_{12}O_{40}]^{5-}$, $[P_2W_{18}O_{62}]^{6-}$) as electron-acceptor units, in the presence of γ-cyclodextrin (γ-CD), which acts as both a supramolecular assembly scaffold and a stabilizing agent. The photoinduced electron-transfer process was investigated using steady-state and time-resolved optical spectroscopy, complemented by spectro-electrochemical measurements, which unambiguously confirm electron transfer from the excited cluster to the POMs. Furthermore, we demonstrate that both the ionic charge of the POMs and the presence of γ-CD significantly influence the efficiency of the process. This work highlights the dual role of γ-CD, which facilitates the association of two negatively charged inorganic units and stabilizes the charge-separated state by maintaining an appropriate spatial arrangement within the supramolecular assembly.

INTRODUCTION.

Among the strategies explored to mitigate the energy crisis, artificial photosynthesis has emerged as a particularly promising direction.[1–7] In that chemical process, photocatalytic materials absorb solar energy and mediate the conversion of water and carbon dioxide into useful fuel molecules.[8–14] Such systems are frequently based on expensive metals (e.g., Ir(III), Ru(II), Pt(II), etc.), or on quantum dots containing toxic elements such as Cd or Pb. These materials combine high efficiency, robustness, and unique electronic properties, making them particularly appealing for specific photocatalytic reactions such as water splitting or CO_2 reduction.[15–22] However, their high cost, environmental

impact, and scalability issues present significant challenges that hinder their widespread implementation.[23,24] Recent efforts have therefore focused on developing alternative systems based on earth-abundant and non-toxic components. In this context, inorganic molecular systems, free of critical raw materials, have emerged as promising alternatives for sustainable photocatalysis.

Octahedral metal atom clusters based on transition elements like molybdenum or tungsten, less expensive than noble metals, constitute a class of electron-rich species that exhibits a strong potential as photosensitizers.[25] Metal atom clusters are formally defined as finite assemblies of metal atoms held together entirely, predominantly, or to a significant extent by metal-metal bonds, even though non-metal atoms may also be intimately associated with the cluster.[26,27] Octahedral, nanometer-sized clusters of transition metals coordinate halogen or chalcogen ligands to give rise to two major structural families: edge-bridged $[\{M_6Q^i_{12}\}X^a_6]$ units and face-capped $[\{M_6Q^i_8\}X^a_6]$ units, where *i* and *a* denote inner and apical ligands, respectively. The intrinsic properties of these M_6 clusters are governed by the nature of the metal, the number of valence electrons, and the identities of both the inner (L^i) and apical (L^a) ligands. Within these families, the face-capped motifs $[\{M_6Q^i_8\}X^a_6]$ (M = Re, Mo, W; Q^i = S, Se, Te and/or Cl, Br, I; X^a = Cl, Br, I) are particularly noteworthy.[27] They display attractive optical and redox characteristics and can generate reactive oxygen species, enabling their use in the design of nanomaterials and functional surfaces with potential applications in lighting, photocatalysis, and biomedical technologies.[28–32,25,33] In particular, halide and mixed-halide face-capped Mo_6 and W_6 clusters- typically formulated as $[\{M_6X^i_8\}X^a_6]^{2-}$ and $[\{M_6X^i_8\}X'^a_6]^{2-}$ (M = Mo, W; X, X' = Cl, Br, I)- exhibit remarkable photophysical behavior, including broad and intense absorption in the UV-visible region, two photons absorption, strong red to near-infrared phosphorescence with quantum yields reaching up to 80%, and long-lived triplet excited states on the microsecond timescale.[34–42]

However, W_6- and Mo_6-based halides often display hydrolytic instability, restricting their aqueous-phase applications and sometimes affecting their physical properties.[43–46] Upon dissolving the cluster

salt in aqueous solution, a pH-dependent hydrolysis occurs, leading to the substitution of the apical ligands by water molecules and/or OH^- groups. The reaction kinetics, however, strongly depend on the nature of the $\{M_6X^i_8\}$ core.[45,47] We selected the $[\{W_6I^i_8\}Cl^a_6]$ motif because the I^i/Cl^a ligand combination endows the cluster with desirable photophysical properties, and tungsten halide clusters are generally less sensitive than their molybdenum analogues to substitution of apical ligands by water molecules. In particular, tungsten clusters exhibit enhanced stability in aqueous media, which motivated the choice of a tungsten-based octahedral halide cluster for this study. Moreover, to enhance the stability of the cluster in aqueous solutions, encapsulation with γ-cyclodextrin (γ-CD) was implemented. γ-CD is a water-soluble macrocycle that is characterized by crown-like hydrophilic outer portals and a hydrophobic internal cavity, making it highly suitable for forming stable inclusion complexes with chaotropic guest anions, like inorganic polyanions.[48–50] Based on this strategy, the host-guest complex $\{[\{W_6I^i_8\}Cl_6]@(\gamma\text{-CD})_2\}^{2-}$ [47] was investigated as a photosensitizing unit in aqueous solution to study the photoinduced electron transfer between $[\{W_6I^i_8\}Cl^a_6]^{2-}$ and polyoxometalates (POMs), while preventing any apical ligand exchanges by water.

POMs are typically described as molecular metal-oxide composed of early transition metals in their highest oxidation states, such as V^{5+}, Mo^{6+}, and W^{6+}, coordinated with oxygen atoms to form a diverse range of atomically precise architectures.[51–56] These metal oxo frameworks function as effective "electron reservoirs", facilitating various redox processes by accepting and donating electrons- a property that underpins their utility in numerous catalytic applications.[55,57–61] As with the cluster component, the selection of the POM composition and structural archetype enables the pre-screening of species with targeted physicochemical properties, tailored to the desired chemical transformation or to the construction of specific supramolecular assemblies. Moreover, their tunable redox potentials can be precisely modulated by varying the POM structure and elemental composition.[60,62,63] However, developing efficient POM-based systems without noble metals for water splitting under visible light remains a major challenge, primarily due to the weak absorption of POMs in the visible range. To

address this limitation, we investigate here the photosensitizing and electron donating capability of the tungsten cluster-based halide $[\{W_6I^i_8\}Cl^a_6]^{2-}$ (Scheme 1A) encapsulated within two γ-CDs (Scheme 1D), in combination with several POMs. This includes Keggin-type anions $[XW_{12}O_{40}]^{n-}$ with X = P^{5+}, Si^{4+}, or B^{3+} (Scheme 1B), and the Dawson-type anion $[P_2W_{18}O_{62}]^{6-}$ (Scheme 1C).

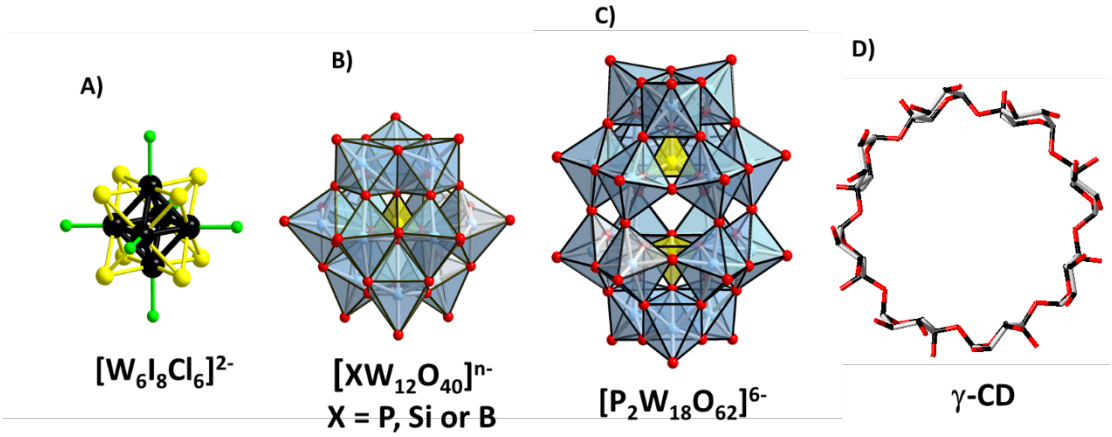

Scheme 1. (A) Structural representation of the tungsten cluster-based halide. Black sphere: W, yellow sphere: I, green sphere: Cl. (B) and (C) Structural representations of the Keggin- and Dawson-type POMs. Blue octahedra: W, yellow tetrahedra: heteroelement X (P, Si or B). (D) Structure of γ-CD.

Using a combination of spectroscopic techniques, we demonstrate that the excited W_6-based motif undergoes efficient photoinduced electron transfer to the POMs. We further assess how the POM charge and the presence of additional γ-CD influence the charge-transfer efficiency. Building on our initial study in organic media,[64] we extend here this investigation to aqueous solution, which reveals the beneficial role of γ-CD, as a supramolecular assembly agent, in modulating the efficiency of the electron-transfer process between the tungsten halide cluster and the POMs.

EXPERIMENTAL SECTION

Materials. Chemicals and solvents for all synthesis and characterization procedures were purchased from Sigma-Aldrich and TCI, and are used as it is. $Na_2\{[\{W_6I^i_8\}Cl^a_6]@(\gamma\text{-CD})_2\}$, $H_3[PW_{12}O_{40}]\cdot 14H_2O$, $H_4[SiW_{12}O_{40}]\cdot 15H_2O$, $H_5[BW_{12}O_{40}]\cdot 10H_2O$ and $K_6[P_2W_{18}O_{62}]\cdot 15H_2O$ were

prepared according to literature procedures[47,65–68] and checked by routine analyses (IR, TGA, EDX, and NMR).

Methods. For photophysical measurements, all sample solutions were thoroughly deoxygenated by purging with argon for at least 20 min to prevent the oxygen-induced quenching of the $\{[\{W_6I^i_8\}Cl^a_6]@(\gamma\text{-CD})_2\}^{2-}$ cluster.

Steady-state absorption and fluorescence spectroscopy. UV-visible steady-state absorption spectroscopy was performed using an Analytik Jena spectrophotometer. The sample concentrations for both absorption and emission measurements were in the micromolar range, and the spectra were recorded in standard quartz cuvettes with a 4 x 10 mm optical path length. Emission spectra were obtained using a Scientific Fluoromax PLUS (Horiba Jobin-Yvon) at room temperature in deaerated 0.1 M $HClO_4$ solution. The presented emission spectra were corrected for the response of both the monochromator and the detector. All samples were excited at 420 nm, with both excitation and emission slit bandpass of 5 nm.

Time-resolved emission spectroscopy. The time-resolved emission measurements were performed using a mid-band (FWHM ~ 4-5 cm^{-1}) optical parametric oscillator (OPO), which was pumped by the 3rd harmonic of a pulsed nanosecond Nd:YAG laser (EKSPLA), as the excitation source, delivering 4 ns pulses at a repetition rate of 10 Hz. After passing through the sample, the emitted light was directed to a spectrograph (SPEX 270M, Jobin-Yvon) via an optical fiber bundle for analysis. The spectrograph dispersed the light, which was then detected by an intensified charge-coupled device (ICCD) camera, PIMAX-4 (Princeton Instrument). The emission kinetics were investigated within the 400 to 700 nm range.

Transient absorption spectroscopy. Laser flash photolysis experiments were conducted using the same EKSPLA laser system described above. The pump laser operated at a repetition rate of 10 Hz, delivering pulses with a width of 4 ns and an energy range of 1-2 mJ per pulse. For transient absorption measurements, a nanosecond white light supercontinuum laser (STM-2-UV LEUKOS)

with a temporal width of less than 1 ns was employed as the probe light. The probe laser was set to a repetition rate of 20 Hz. To monitor spectral energy distribution fluctuations, the probe beam was split by a beam splitter, directing one part of the beam to the sample cell and the other to a reference. The transmitted light from the sample entered the center of a round-to-linear optical fiber bundle, which guided the light to a spectrograph (SPEX 270M, Jobin-Yvon) for spectral analysis. The dispersed white light from the spectrograph was detected by an intensified charge-coupled device (ICCD) camera (PIMAX-4, Princeton Instrument), which was synchronized with both the pump and probe lasers. The spectrograph simultaneously recorded spectra from both the reference and the sample.

Using Equation (1), difference absorption spectra can be recorded by varying the delay time between pump and probe:

$$\Delta A = log_{10}\left(\frac{s_{ref}^{p}}{s_{ref}^{0}} \times \frac{s_{sample}^{0}}{s_{sample}^{p}}\right) \qquad (1)$$

where s_{ref}^{p} and s_{ref}^{0} are reference spectra when the pump is on and off, respectively, while s_{sample}^{p} and s_{sample}^{0} are sample spectra when the pump is on and off, respectively. All measurements were taken with a quartz cuvette of 4 mm x 10 mm dimension.

Electrochemical measurements. Cyclic voltammetry (CV) experiments were conducted using a compact PalmSens4 potentiostat, controlled by a computer via Nova software. All measurements were performed at room temperature in a single-compartment micro-cell. A glassy carbon (GC) electrode with a 2 mm diameter was employed as the working electrode, while a graphite electrode served as the auxiliary electrode. Potentials were quoted against an Ag wire reference electrode, and all values are referenced to the ferrocene/ferrocenium internal standard. Electrochemical measurements were carried out in 0.1 M $HClO_4$, acting as the supporting electrolyte. Prior to the experiments, all solutions were purged with argon for at least 20 min to remove oxygen, and they were kept under a positive argon pressure throughout the experiment. The potentials determined from

the CV ($[PW_{12}O_{40}]^{3-}$: 0.1 V, $[SiW_{12}O_{40}]^{4-}$: -0.2 V, $[BW_{12}O_{40}]^{5-}$: -0.4 V, $[P_2W_{18}O_{62}]^{6-}$: 0.1 V) were used to conduct chronoamperometry with the same working, reference and auxiliary electrodes of the previously described cell system. To ensure complete oxidation/reduction, the samples were quantitatively oxidized or reduced stepwise using controlled potential coulometry. Linear scan voltammetry measurements were performed at each coulometric step (before and after reduction) with a rotating disk electrode to confirm complete reduction/oxidation. The reduced POM solutions were subsequently analysed using a Perkin Elmer Lambda 750 UV-Vis-NIR spectrophotometer.

RESULT and DISCUSSION.

Steady-state absorption and emission measurements of $\{[\{W_6I^i_8\}Cl^a_6]@(\gamma\text{-CD})_2\}^{2-}$ cluster. The absorption and emission spectra of the host-guest complex $\{[\{W_6I^i_8\}Cl^a_6]@(\gamma\text{-CD})_2\}^{2-}$ are presented in Fig. 1A. The host-guest complex displays an intense absorption band in the ultraviolet (UV) region centered around 326 nm, which extends into the visible range up to approximately 450 nm. The signature of the host-guest complex is dominated by the optical properties of $[\{W_6I^i_8\}Cl^a_6]^{2}$, which exhibit ligand-to-metal charge-transfer (LMCT) transitions in the near-ultraviolet region.[69]

Upon excitation of $\{[\{W_6I^i_8\}Cl^a_6]@(\gamma\text{-CD})_2\}^{2-}$ at 420 nm in deaerated 0.1 M $HClO_4$, a broad emission band centered near 670 nm is observed, with a quantum yield of 0.11 ± 0.01, in good agreement with the reported values.[47] This emission spans the red and near-infrared regions and is similar to the behavior of $[\{W_6I^i_8\}Cl^a_6]^{2-}$ in acetonitrile, as previously reported by Gray and coworkers.[70] The emission intensity and spectral position suggest that the inclusion within the γ-CD cavity does not significantly alter the emissive properties of $[\{W_6I^i_8\}Cl^a_6]^{2-}$, underscoring its chemical robustness and the preservation of its electronic structure upon encapsulation. On the other hand, POMs display either negligible or weak absorption in the visible region (Fig. 1B). Their characteristic LMCT bands, originating from oxygen-to-tungsten (O→W) transitions within tungsten-oxo frameworks, are predominantly observed in the UV region.[71]

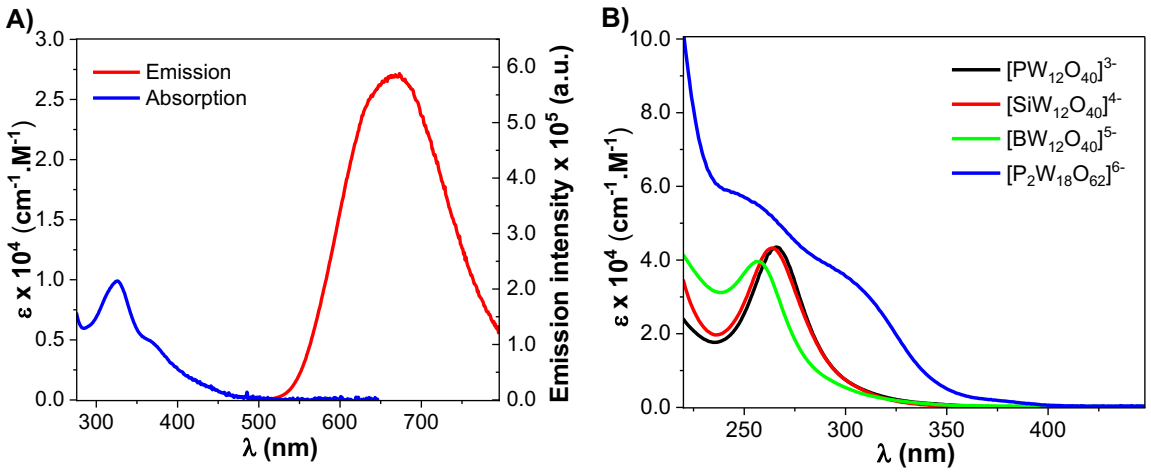

Figure 1. (A) Steady-state absorption (blue) and emission (red) spectra of 40 μM aqueous solution of $\{[\{W_6I^i_8\}Cl^a_6]@(\gamma\text{-CD})_2\}^{2-}$, and (B) steady-state absorption of POMs in 0.1 M $HClO_4$

Time-resolved spectroscopic measurements of $\{[\{W_6I^i_8\}Cl^a_6]@(\gamma\text{-CD})_2\}^{2-}$ cluster. Time-resolved emission measurements of the cluster were performed upon excitation at 420 nm. The excited-state lifetime was determined by mono-exponential fitting of the kinetic trace at 650 nm, yielding a value of 9.7 ± 0.6 μs (inset of Fig. 2A). This value aligns closely with the previously reported data by Gray et *al*. (10 μs),[70] confirming the consistency of the photophysical behavior of the cluster. In aerated solutions, the excited-state lifetime decreased significantly to 4.0 ± 0.4 μs due to O_2 induced quenching (Fig. 2B), confirming the triplet nature of the excited state.

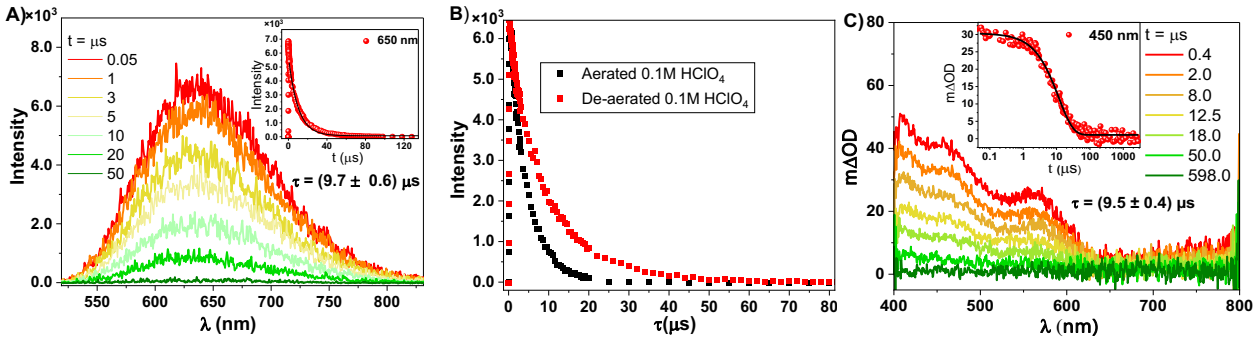

Figure 2. (A) Time-resolved emission spectra, (B) time-resolved emission decays, and (C) nanosecond transient absorption spectra of 200 μM of $\{[\{W_6I^i_8\}Cl^a_6]@(\gamma\text{-CD})_2\}^{2-}$ in 0.1 M $HClO_4$. Pump fluence = 9 mJ/cm^2 at λ_{exc} = 420 nm.

The transient absorption (TA) spectra (Fig. 2C) were recorded under identical excitation conditions. They reveal characteristic features of the triplet-excited state across the visible range, with a pronounced absorption maximum at approximately 400 nm. The triplet excited-state lifetime was determined by monoexponential global fitting of the TA kinetic traces, yielding a value of 9.5 ± 0.4 μs, in excellent agreement with the emission lifetime. This concordance reinforces the reliability of the experimental approach used for the photophysical characterization of $[\{W_6I^i_8\}Cl^a_6]^{2-}$. Understanding the photophysical properties of this triplet state is essential for exploring the cluster's potential in triplet-mediated photochemical applications.

Quenching of $\{[\{W_6I^i_8\}Cl^a_6]@(\gamma\text{-CD})_2\}^{2-}$ by POMs. The quenching behavior of the excited state of $\{[\{W_6I^i_8\}Cl^a_6]@(\gamma\text{-CD})_2\}^{2-}$ by POMs as electron acceptors was systematically investigated to elucidate the dynamics of the photoinduced electron transfer (PET) reactions. Quenching rate constants were determined through steady-state and time-resolved emission measurements at varying POM concentrations in argon-saturated 0.1 M $HClO_4$. The Stern-Volmer (SV) relationship was employed to analyse the quenching efficiency, using the equations $\tau_0/\tau = 1 + k_{sv}[Q]$ or $I_0/I = 1 + k_{sv}[Q]$, where τ_0 and I_0 are the emission lifetime and intensity in the absence of quencher, respectively, and [Q] is the quencher concentration. The quenching constant (k_q) was determined using $k_q = k_{sv}/\tau_0$. Upon the addition of $[PW_{12}O_{40}]^{3-}$, $[SiW_{12}O_{40}]^{4-}$, $[BW_{12}O_{40}]^{5-}$, and $[P_2W_{18}O_{62}]^{6-}$, a gradual decrease in both emission intensity and lifetime of $[\{W_6I^i_8\}Cl^a_6]^{2-}$ was observed (Figures S1, S2, S3 and S4). Linear fitting of Stern-Volmer plots (Fig. S5) obtained for all POMs in both steady-state (I_0/I) and time-resolved (τ_0/τ) measurements results in very similar Stern-Volmer constants, consistent with a dynamic quenching mechanism. The Stern-Volmer constants (k_{sv}) and quenching rate constants (k_q) for the interaction of $[\{W_6I^i_8\}Cl^a_6]^{2-}$ with POMs obtained from time-resolved measurements are summarized in Table 1 and those from steady-state measurements are listed in Table S1. These parameters provide crucial quantitative metrics for evaluating the efficiency of the quenching process mediated by the POMs.

Table 1. POM volume charge density[a] (VCD) and standard reduction potential[b] (E_{red}), and Stern-Volmer and quenching rate constants (k_{sv} and k_q) determined from time-resolved emission lifetime decay by POM

POMs	**VCD[a] (C.cm^{-3})**	**E_{red}[b] (V)**	**k_{sv} (M^{-1})**	**k_q x 10^9 ($M^{-1}s^{-1}$)**
$[PW_{12}O_{40}]^{3-}$	827	0.13	17989	1.93
$[P_2W_{18}O_{62}]^{6-}$	1060	0.12	14860	1.60
$[SiW_{12}O_{40}]^{4-}$	1103	-0.10	13237	1.43
$[BW_{12}O_{40}]^{5-}$	1379	-0.36[c]	11516	1.24

[a]Volume charge density estimated based on the volume of the POMs (581 Å^3 for Keggin anions; 907 Å^3 for Dawson anion), [b]The first standard potential of the POM (V vs. Fc/Fc$^+$) measured by CV in 0.1 M $HClO_4$, [c]measured in acetate buffer at pH = 5 (see Fig. S6, ESI).

Among the studied POMs, $[PW_{12}O_{40}]^{3-}$ demonstrates the highest Stern-Volmer constant (k_{sv} = 17989 M^{-1}) and bimolecular quenching rate constant (k_q = 1.93×10^9 $M^{-1}s^{-1}$), which can be attributed to its highest redox potential (E_{red} = 0.13 V vs Fc/Fc$^+$) and lowest volume charge density (VCD = 827 C.cm^{-3}). The first standard reduction potential (E_{red}) of POMs, determined using cyclic voltammetry (Fig. S6), reflects the POM's ability to accept electrons. It plays a crucial role in determining quenching efficiency. A higher E_{red} increases the thermodynamic driving force for electron transfer from the excited state of the donor ($[\{W_6I^i_8\}Cl^a_6]^{2-}$) to the acceptor (POM). Furthermore, the low volume charge density minimizes the Coulombic repulsion between the POM and $[\{W_6I^i_8\}Cl^a_6]^{2-}$, which are both negatively charged, and thus facilitates dynamic quenching. In contrast, POMs with higher volume charge densities exhibit reduced quenching efficiencies following the trend $[PW_{12}O_{40}]^{3-}$ > $[SiW_{12}O_{40}]^{4-}$ > $[BW_{12}O_{40}]^{5-}$ among Keggin-type POMs. This tendency is consistent with the greater electrostatic repulsion between negatively charged POMs and $[\{W_6I^i_8\}Cl^a_6]^{2-}$, which hinders effective interaction. Interestingly, the Dawson-type POM $[P_2W_{18}O_{62}]^{6-}$ demonstrates a higher quenching constant (k_q = 1.60×10^9 $M^{-1}s^{-1}$) than $[SiW_{12}O_{40}]^{4-}$ (k_q = 1.43×10^9 $M^{-1}s^{-1}$) despite having a similar charge

density. This deviation may stem from the intrinsic electronic properties of $[P_2W_{18}O_{62}]^{6-}$, which is a stronger electron acceptor than $[SiW_{12}O_{40}]^{4-}$, as evidenced by the more positive potential of its first redox wave.

Effect of γ-CD concentration. To evaluate the effect of γ-CD, known for its ability to assemble POMs and clusters into a single supramolecular entity referred to as a CLUSPOM,[72,73] we further investigated the photophysical behavior of these systems as a function of γ-CD concentration. Initially, the $\{[\{W_6I^i_8\}Cl^a_6]@(\gamma\text{-CD})_2\}^{2-}$ cluster-based inclusion complex was characterized alone by incrementally increasing the γ-CD concentration (see Fig. S10). No significant changes in emission intensity or lifetime were observed, indicating that the host-guest assembly between $[\{W_6I^i_8\}Cl^a_6]^{2-}$ and γ-CD is already optimized. This optimized assembly involves one $[\{W_6I^i_8\}Cl^a_6]^{2-}$ unit deeply encapsulated by two γ-CD molecules, as observed in the solid state, forming a 1:2 sandwich complex.[47,50] Consequently, further addition of γ-CD does not enhance the shielding of the cluster from the surrounding solvent environment.

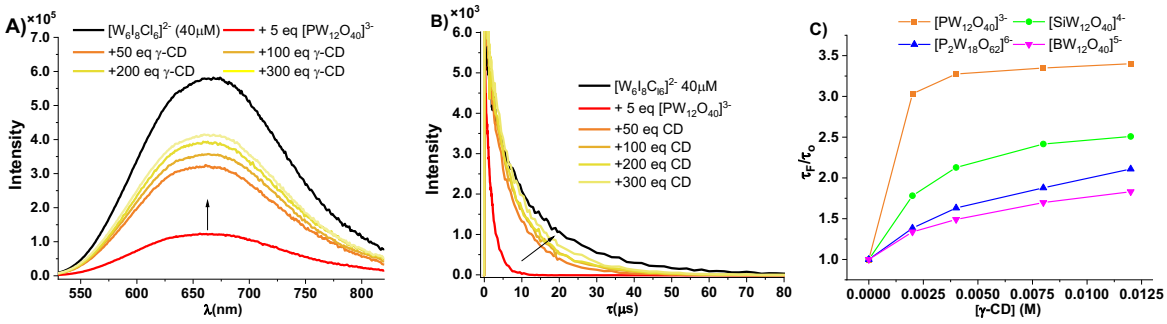

Figure 3. (A) Steady-state emission spectra, and (B) time-resolved emission decays of 40 μM of $\{[\{W_6I^i_8\}Cl^a_6]@(\gamma\text{-CD})_2\}^{2-}$ and 200 μM of $[PW_{12}O_{40}]^{3-}$ at increasing concentration of γ-CD in Ar-saturated 0.1 M $HClO_4$. (C) Ratio of the emission lifetime as a function of the γ-CD concentration in the 40 μM $\{[\{W_6I^i_8\}Cl^a_6]@(\gamma\text{-CD})_2\}^{2-}$ and 200 μM POM system (see text for details).

We next assessed how increasing γ-CD concentration affects the quenching efficiency of $\{[\{W_6I^i_8\}Cl^a_6]@(\gamma\text{-CD})_2\}^{2-}$ by POMs by measuring the emission intensity and lifetime of aqueous

solutions containing $\{[\{W_6I^i_8\}Cl^a_6]@(\gamma\text{-CD})_2\}^{2-}$-POM with varying γ-CD concentrations. As shown in Fig. 3A and 3B, the addition of 5 equivalents of $[PW_{12}O_{40}]^{3-}$ to the 40 μM aqueous solution of $\{[\{W_6I^i_8\}Cl^a_6]@(\gamma\text{-CD})_2\}^{2-}$ led to a ~6-fold decrease in both emission intensity and lifetime. Subsequent addition of 50 equivalents of γ-CD to this solution caused an increase in both emission intensity and lifetime. Further increases in γ-CD concentration led to gradual recovery of intensity and lifetime, although full restoration was not achieved even at 300 equivalents of γ-CD. Similar experiments with $[SiW_{12}O_{40}]^{4-}$, $[BW_{12}O_{40}]^{5-}$ and $[P_2W_{18}O_{62}]^{6-}$ (Figures S7, S8 and S9) showed consistent enhancement in both emission intensities and lifetimes, though the magnitude of the effect varied, suggesting differences in responsiveness to γ-CD. These observations can be attributed to the interactions between the POMs and the hydrophobic cavities of γ-CD,[74,75] consistent with recent findings showing that such nanoconfinement significantly suppresses the ability of POMs to undergo intermolecular electron transfer.[76] This likely increases the spatial separation between the cluster and the POM units, thereby reducing emission quenching. As γ-CD concentration increases, POMs can form encapsulated complexes with γ-CD at different stoichiometries, depending on the concentration of γ-CD and their binding constants.[75]

We further examined the correlation between the γ-CD concentration and the emission lifetime ratio τ_F/τ_0, where τ_0 is the emission lifetime of $\{[\{W_6I^i_8\}Cl^a_6]@(\gamma\text{-CD})_2\}^{2-}$ with 5 equivalents of POM, and τ_F is the lifetime after adding a given amount of γ-CD. As shown in Fig. 3C, τ_F/τ_0 increases for all POMs, with the highest enhancement observed for $[PW_{12}O_{40}]^{3-}$ (ratio ~3.5 at 100-300 equivalents γ-CD) and the lowest for $[BW_{12}O_{40}]^{5-}$, suggesting reduced sensitivity to γ-CD. These trends are consistent with the previous study on the binding behavior of POM with γ-CD, in which the global charge density of the polyanions was varied.[75] The interaction between POM and γ-CD occurs through various recognition modes, which are strongly influenced by the chaotropic effect of the POMs and correlate with their binding constants. The Keggin-type POM $[BW_{12}O_{40}]^{5-}$ with a high

ionic charge exhibits only weak interactions with the outer surface of the γ-CD without host-guest encapsulation (binding constant $K_{1:1}$ = 600 M^{-1}). Further reduction of the ionic charge to $[SiW_{12}O_{40}]^{4-}$ results in the formation of 1:1 and 1:2 inclusion complexes, accompanied by higher binding constants ($K_{1:1}$ = 9500 M^{-1}, $K_{1:2}$ = 150 M^{-1}).[75] At the lowest ionic charge, $[PW_{12}O_{40}]^{3-}$ exhibits the strongest binding associations ($K_{1:1}$ = 90000 M^{-1}, $K_{1:2}$ = 1500 M^{-1}).[75] The Dawson-type POM $[P_2W_{18}O_{62}]^{6-}$ also exhibited a two-step complexation process without true encapsulation due to host-guest size mismatch, leading to only moderate binding constants ($K_{1:1}$ = 3200 M^{-1}, $K_{1:2}$ = 370 M^{-1}).[77] As the chaotropic character of POM can be evaluated with respect to their ability to bind to γ-CD, and thus to the values of the binding constants, the screening effect of γ-CD should increase following the order: $[BW_{12}O_{40}]^{5-}$ < $[P_2W_{18}O_{62}]^{6-}$ < $[SiW_{12}O_{40}]^{4-}$ < $[PW_{12}O_{40}]^{3-}$. The stronger the affinity towards the γ-CD, the greater the isolation of $[\{W_6I^i_8\}Cl^a_6]^{2-}$ and POM units, and therefore the lower the emission quenching efficiency. Consequently, the electron transfer efficiency in cluster-POM tandems can also be tuned by varying the concentration of γ-CD unit.

Transient absorption spectroscopy of CLUSPOM systems. Nanosecond transient absorption spectroscopy was employed to gain a deeper understanding of the charge transfer and recombination dynamics of the $\{[\{W_6I^i_8\}Cl^a_6]@(\gamma\text{-CD})_2\}^{2-}$ cluster-based inclusion complex in the presence of POM, with varying concentrations of γ-CD. Transient absorption spectra of $\{[\{W_6I^i_8\}Cl^a_6]@(\gamma\text{-CD})_2\}^{2-}$ in the presence of 5 equivalents of $[P_2W_{18}O_{62}]^{6-}$ were recorded in an argon-saturated aqueous solution (Fig. 4A).

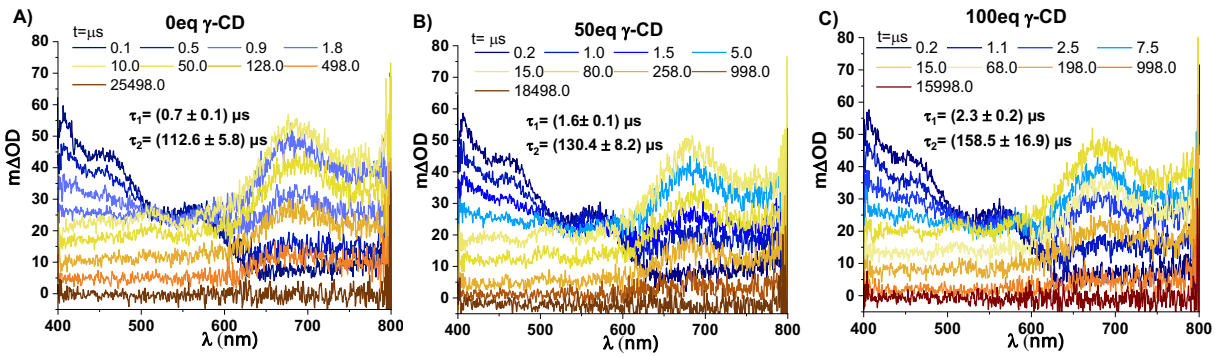

Figure 4. Nanosecond transient absorption spectra of 200 μM of $\{[\{W_6I^i_8\}Cl^a_6]@(\gamma\text{-CD})_2\}^{2-}$ in the presence of 5 equivalents of $[P_2W_{18}O_{62}]^{6-}$ with A) 0, B) 50 and C) 100 equivalents of γ-CD in argon-saturated 0.1 M $HClO_4$. Pump fluence = 9 mJ/cm^2 at λ_{exc} = 420 nm.

Upon excitation at 420 nm, a characteristic TA signal with maximum absorption at approximately 400 nm, attributed to the excited state of the $\{[\{W_6I^i_8\}Cl^a_6]^{2-}$ motif, was observed at 100 ns. Beyond, the signal gradually decayed, accompanied by the emergence of a new broad transient band spanning the visible range, with an absorption maximum around 700 nm. Global fitting of the TA kinetic traces (Fig. S14A) revealed two time constants: 0.7 ± 0.1 μs, corresponding to the formation of the charge-separated state, and 112.6 ± 5.8 μs, associated with charge recombination (see the decay-associated differential spectra (DADS) in Fig. S15A).

The subsequent addition of 50 and 100 equivalents of γ-CD to the 1:5 mixture of $\{[\{W_6I^i_8\}Cl^a_6]@(\gamma\text{-CD})_2\}^{2-}$ and $[P_2W_{18}O_{62}]^{6-}$ resulted in transient absorption features similar to those observed for the in the initial mixture (Figures 4B and 4C). However, global fitting of the kinetic traces revealed slightly modified time constants: 1.6 ± 0.1 μs and 130.4 ± 8.2 μs for 50 equivalents γ-CD and 2.3 ± 0.2 μs and 158.5 ± 16.9 μs for 100 equivalents. The increase in the first time constant associated with the electron transfer process, suggests that increasing γ-CD concentration hinders electron transfer, due to enhanced shielding or increased spatial separation between $\{[\{W_6I^i_8\}Cl^a_6]^{2-}$ and the POM by γ-CD. Although the complexation of POMs by CDs is known to slightly shift their first reduction potential, making them more difficult to reduce,[75] the spatial separation between the donor and the acceptor should also contribute to the increases in these characteristic times. Indeed, the increased time constant for charge recombination indicates a slower back-electron-transfer process.

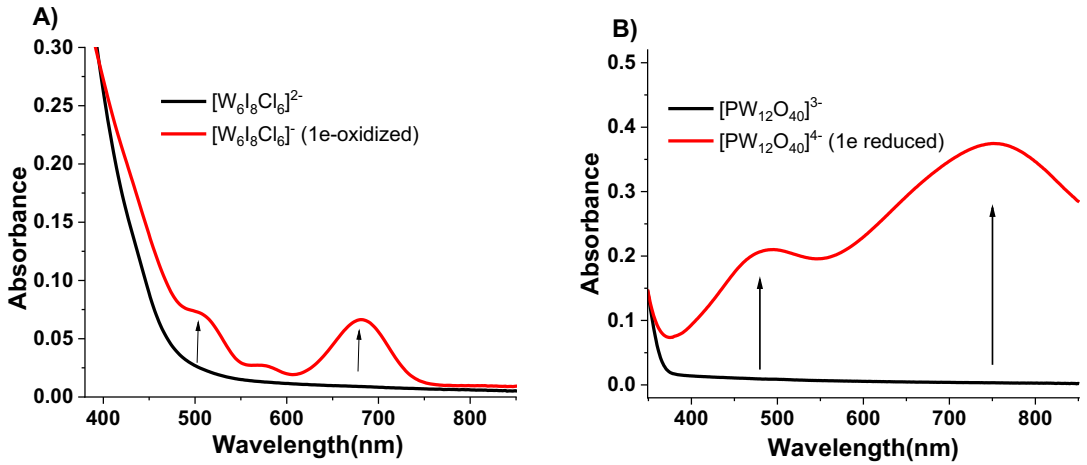

Figure 5. Absorption spectra of (A) parent and one-electron oxidized cluster and (B) parent and one-electron reduced POM. Reference electrode: Ag wire; working electrode: porous carbon and auxiliary electrode: graphite carbon; electrolyte: 0.1 M $HClO_4$.

Similar experiments performed with the cluster-Keggin POM systems produced comparable nanosecond transient absorption spectra (see Figures S11, S12 and S13), and global fitting of their TA kinetic traces (Figures S14B to D) revealed time constants of the same order of magnitude, corresponding to the formation of the charge-separated state, followed by the charge recombination (DADS in Figures S15B to D).

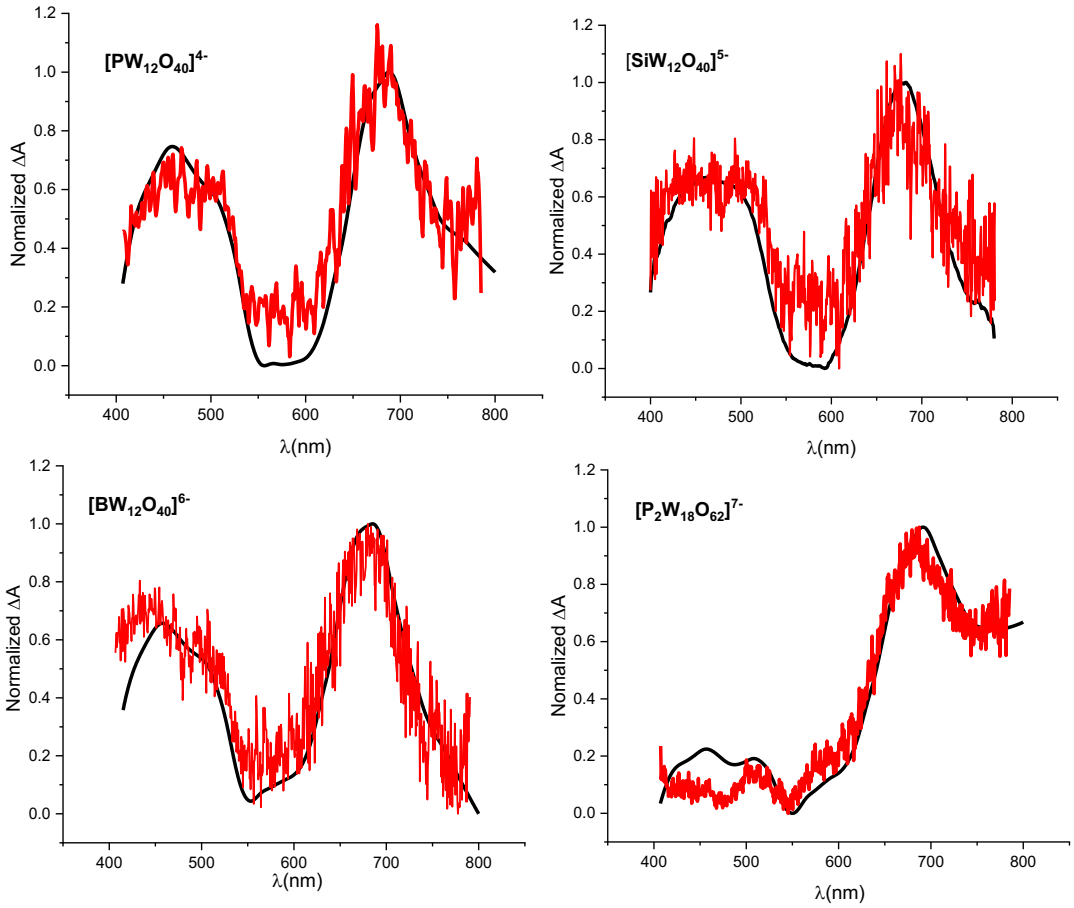

Figure 6. Comparison of spectro-electrochemical spectra (black: sum of one-electron oxidized cluster and one-electron reduced POM spectra) with nanosecond transient absorption spectra (red) observed for the charge-separated state.

To confirm the photoinduced electron transfer from $\{[\{W_6I^i_8\}Cl^a_6]^{2-}$ to the POMs, the spectro-electrochemical behavior of the reduced polyoxometalates and the oxidized cluster was investigated in 0.1 M $HClO_4$ by applying potentials determined via cyclic voltammetry ($[PW_{12}O_{40}]^{3-}$: 0.1 V, $[SiW_{12}O_{40}]^{4-}$: -0.2 V, $[BW_{12}O_{40}]^{5-}$: -0.4 V, $[P_2W_{18}O_{62}]^{6-}$: 0.1 V and $\{[\{W_6I^i_8\}Cl^a_6]^{2-}$: 1.2 V). All POMs were quantitatively reduced to yield one-electron reduced species (Fig. 5B and Fig. S16). The Keggin-type POMs used in this study exhibit a broad absorption band spanning the visible to near-infrared region, characteristic of the intervalence charge transfer bands of reduced POMs. The oxidized $\{[\{W_6I^i_8\}Cl^a_6]@(\gamma\text{-CD})_2\}^-$ inclusion complex exhibits two prominent absorption bands at

approximately 500 and 680 nm, leading to a noticeable colour change from yellow to brown (Fig. 5A).

Photoinduced electron transfer was confirmed by comparing the TA spectra at the delay time corresponding to the maximum formation of the charge-separated state with the linear combination of the spectroelectrochemical spectra of the one-electron-oxidized cluster and one-electron-reduced POMs (Fig. 6). In all cases, we observe almost perfect correspondence between the transient absorption spectroscopic features and the linear combination of the spectro-electrochemical difference spectra of the oxidized cluster-based motif $\{[\{W_6I^i_8\}Cl^a_6]^-$ and reduced POM (Fig. 6). This result confirms that photoinduced electron transfer occurs from the triplet excited state of $\{[\{W_6I^i_8\}Cl^a_6]@(\gamma\text{-CD})_2\}^{2-}$ to the POMs.

CONCLUSION

In this study, we first investigated the quenching behavior in aqueous solution of the excited state of the tungsten halide cluster-based motif, namely $[\{W_6I^i_8\}Cl^a_6]^{2-}$, encapsulated with two cyclodextrins, forming the host-guest complex $\{[\{W_6I^i_8\}Cl^a_6]@(\gamma\text{-CD})_2\}^{2-}$, in the presence of polyoxometalates with varying charges and redox potentials. The resulting quenching rate constants revealed a strong dependence on both the charge density and reduction potential of the POMs, which in turn modulate the rate of photoinduced electron transfer. To further explore the influence of host-guest interactions with cyclodextrin introduced to stabilize the charge-separated state, we examined the effect of γ-CD concentration on electron transfer efficiency in cluster-POM solutions. The results suggest that the interaction between POM and γ-CD occurs through various recognition modes, strongly modulated by the chaotropic character of the POMs, as reflected in their binding constants. These observations were also supported by transient absorption studies, which revealed systematic increases in both charge-separation formation and charge-recombination lifetimes upon γ-CD addition. Overall, this work demonstrates that fine-tuning the electron transfer efficiency in CLUSPOM systems can be achieved by modulating the POM's redox potential, charge density, and supramolecular environment.

These insights not only deepen the understanding of charge-transfer processes in sophisticated supramolecular systems but also provide guidelines for the development of robust, earth-abundant photosensitizer-catalyst systems for sustainable energy conversion applications.

ACKNOWLEDGMENTS

This work was supported by CLUSPOM-H2 project (ANR-22-CE50-0007-01). We acknowledge the French Embassy in Vietnam for financial support through the France Excellence scholarship awarded to Thi Huyen My Dang.

ASSOCIATED CONTENT

Supporting Information. Additional photophysical characterizations including steady-state absorption and emission as well as time-resolved emission measurements upon addition of different POMs; Stern-Volmer plots and corresponding quenching rate constants; steady-state and time-resolved emission and transient absorption measurements in the presence of γ-CD; decay-associated difference spectra obtained from TAS; cyclic voltammograms (CV); and spectro-electrochemical difference spectra (PDF).

AUTHOR INFORMATION

Corresponding Author

Minh-Huong Ha-Thi

Université Paris-Saclay, CNRS, Institut des Sciences Moléculaires d'Orsay (ISMO), 91405 Orsay, France.

Email : minh-huong.ha-thi@universite-paris-saclay.fr

Thomas Pino

Université Paris-Saclay, CNRS, Institut des Sciences Moléculaires d'Orsay (ISMO), 91405 Orsay, France.

Email: thomas.pino@cnrs.fr

Mohamed Haouas

Université de Versailles Saint-Quentin-en-Yvelines, CNRS, Institut Lavoisier de Versailles (ILV), 78035, Versailles Cedex, France.

Email: mohamed.haouas@uvsq.fr

Stéphane Cordier

Université de Rennes, CNRS, Institut des Sciences Chimiques de Rennes (ISCR), 35000 Rennes, France.

Email: stephane.cordier@univ-rennes.fr

Author Contributions

The manuscript was written through contributions of all authors. All authors have given approval to the final version of the manuscript.

REFERENCES

(1) Barber, J.; Tran, P. D. From Natural to Artificial Photosynthesis. *J. R. Soc. Interface* **2013**, *10* (81), 20120984. https://doi.org/10.1098/rsif.2012.0984.
(2) Thapper, A.; Styring, S.; Saracco, G.; Rutherford, A. W.; Robert, B.; Magnuson, A.; Lubitz, W.; Llobet, A.; Kurz, P.; Holzwarth, A. R.; Fiechter, S.; Groot, H. J. M. de; Campagna, S.; Braun, A.; Bercegol, H.; Artero, V. Artificial Photosynthesis for Solar Fuels: An Evolving Research Field within AMPEA, a Joint Programme of the European Energy Research Alliance. *Green* **2013**, *3* (1), 43–57. https://doi.org/10.1515/green-2013-0007.
(3) Kuang, T. A Breakthrough of Artificial Photosynthesis. *Natl. Sci. Rev.* **2016**, *3* (1), 2–3. https://doi.org/10.1093/nsr/nwv071.
(4) Zhang, B.; Sun, L. Artificial Photosynthesis: Opportunities and Challenges of Molecular Catalysts. *Chem. Soc. Rev.* **2019**, *48* (7), 2216–2264. https://doi.org/10.1039/C8CS00897C.

(5) El-Khouly, M. E.; El-Mohsnawy, E.; Fukuzumi, S. Solar Energy Conversion: From Natural to Artificial Photosynthesis. *J. Photochem. Photobiol. C Photochem. Rev.* **2017**, *31*, 36–83. https://doi.org/10.1016/j.jphotochemrev.2017.02.001.
(6) Wang, Z.; Hu, Y.; Zhang, S.; Sun, Y. Artificial Photosynthesis Systems for Solar Energy Conversion and Storage: Platforms and Their Realities. *Chem. Soc. Rev.* **2022**, *51* (15), 6704–6737. https://doi.org/10.1039/D1CS01008E.
(7) Najafpour, M. M.; Shen, J.-R.; Allakhverdiev, S. I. Natural and Artificial Photosynthesis: Fundamentals, Progress, and Challenges. *Photosynth. Res.* **2022**, *154* (3), 229–231. https://doi.org/10.1007/s11120-022-00982-z.
(8) Tachibana, Y.; Vayssieres, L.; Durrant, J. R. Artificial Photosynthesis for Solar Water-Splitting. *Nat. Photonics* **2012**, *6* (8), 511–518. https://doi.org/10.1038/nphoton.2012.175.
(9) Liu, C.; Dasgupta, N. P.; Yang, P. Semiconductor Nanowires for Artificial Photosynthesis. *Chem. Mater.* **2014**, *26* (1), 415–422. https://doi.org/10.1021/cm4023198.
(10) Kudo, A.; Miseki, Y. Heterogeneous Photocatalyst Materials for Water Splitting. *Chem. Soc. Rev.* **2008**, *38* (1), 253–278. https://doi.org/10.1039/B800489G.
(11) Liao, L.; Zhang, Q.; Su, Z.; Zhao, Z.; Wang, Y.; Li, Y.; Lu, X.; Wei, D.; Feng, G.; Yu, Q.; Cai, X.; Zhao, J.; Ren, Z.; Fang, H.; Robles-Hernandez, F.; Baldelli, S.; Bao, J. Efficient Solar Water-Splitting Using a Nanocrystalline CoO Photocatalyst. *Nat. Nanotechnol.* **2014**, *9* (1), 69–73. https://doi.org/10.1038/nnano.2013.272.
(12) Kibria, M. G.; Chowdhury, F. A.; Zhao, S.; AlOtaibi, B.; Trudeau, M. L.; Guo, H.; Mi, Z. Visible Light-Driven Efficient Overall Water Splitting Using p-Type Metal-Nitride Nanowire Arrays. *Nat. Commun.* **2015**, *6* (1), 6797. https://doi.org/10.1038/ncomms7797.
(13) Li, K.; Peng, B.; Peng, T. Recent Advances in Heterogeneous Photocatalytic CO_2 Conversion to Solar Fuels. *ACS Catal.* **2016**, *6* (11), 7485–7527. https://doi.org/10.1021/acscatal.6b02089.
(14) Albero, J.; Peng, Y.; García, H. Photocatalytic CO_2 Reduction to C_{2+} Products. *ACS Catal.* **2020**, *10* (10), 5734–5749. https://doi.org/10.1021/acscatal.0c00478.
(15) Koike, T.; Akita, M. Visible-Light Radical Reaction Designed by Ru- and Ir-Based Photoredox Catalysis. *Inorg. Chem. Front.* **2014**, *1* (8), 562–576. https://doi.org/10.1039/C4QI00053F.
(16) Sawaki, T.; Ishizuka, T.; Namura, N.; Hong, D.; Miyanishi, M.; Shiota, Y.; Kotani, H.; Yoshizawa, K.; Jung, J.; Fukuzumi, S.; Kojima, T. Photocatalytic Hydrogen Evolution Using a Ru(II)-Bound Heteroaromatic Ligand as a Reactive Site. *Dalton Trans.* **2020**, *49* (47), 17230–17242. https://doi.org/10.1039/D0DT03546G.
(17) Shimoyama, Y.; Koga, K.; Tabe, H.; Yamada, Y.; Kon, Y.; Hong, D. RuO_2 Nanoparticle-Embedded Graphitic Carbon Nitride for Efficient Photocatalytic H_2 Evolution. *ACS Appl. Nano Mater.* **2021**, *4* (11), 11700–11708. https://doi.org/10.1021/acsanm.1c02301.
(18) Ohira, R.; Naya, S.; Fujishima, M.; Tada, H. Interfacial Interaction between the Ruthenium(IV) Oxide Cluster and Graphitic Carbon Nitride Governing the Photocatalytic Activity. *J. Phys. Chem. C* **2023**, *127* (45), 22076–22084. https://doi.org/10.1021/acs.jpcc.3c05867.
(19) Qiu, S.; Shen, Y.; Wei, G.; Yao, S.; Xi, W.; Shu, M.; Si, R.; Zhang, M.; Zhu, J.; An, C. Carbon Dots Decorated Ultrathin CdS Nanosheets Enabling In-Situ Anchored Pt Single Atoms: A Highly Efficient Solar-Driven Photocatalyst for Hydrogen Evolution. *Appl. Catal. B Environ.* **2019**, *259*, 118036. https://doi.org/10.1016/j.apcatb.2019.118036.
(20) Zhang, Z.; Li, L.; Jiang, Y.; Xu, J. Step-Scheme Photocatalyst of $CsPbBr_3$ Quantum Dots/BiOBr Nanosheets for Efficient CO_2 Photoreduction. *Inorg. Chem.* **2022**, *61* (7), 3351–3360. https://doi.org/10.1021/acs.inorgchem.2c00012.
(21) Wang, Y.; Wang, Q.; Jiang, G.; Zhang, Q.; Wang, J.; Li, Z. CsPbBr3 Nanocrystals Stabilized by Lead Oxysalts for Photocatalytic CO_2 Reduction. *ACS Appl. Nano Mater.* **2023**, *6* (7), 5087–5092. https://doi.org/10.1021/acsanm.3c00273.
(22) Li, W.; Zhang, Y.; Tian, F.; Tian, J.; Ran, W.; Zhang, D.; Li, N.; Yan, T. Pt/BiOBr Nanocomposite Supported on Graphdiyne for the Selective Photoreduction of CO_2 into

Hydrocarbons. *ACS Appl. Nano Mater.* **2024**, *7* (14), 16659–16668. https://doi.org/10.1021/acsanm.4c02728.
(23) Djurišić, A. B.; He, Y.; Ng, A. M. C. Visible-Light Photocatalysts: Prospects and Challenges. *APL Mater.* **2020**, *8* (3), 030903. https://doi.org/10.1063/1.5140497.
(24) Liang, Z.; Yin, L.; Yin, H.; Yin, Z.; Du, Y. Rare Earth Element Based Single-Atom Catalysts: Synthesis, Characterization and Applications in Photo/Electro-Catalytic Reactions. *Nanoscale Horiz.* **2021**, *7* (1), 31–40. https://doi.org/10.1039/D1NH00459J.
(25) Renaud, A.; Grasset, F.; Dierre, B.; Uchikoshi, T.; Ohashi, N.; Takei, T.; Planchat, A.; Cario, L.; Jobic, S.; Odobel, F.; Cordier, S. Inorganic Molybdenum Clusters as Light-Harvester in All Inorganic Solar Cells: A Proof of Concept. *ChemistrySelect* **2016**, *1* (10), 2284–2289. https://doi.org/10.1002/slct.201600508.
(26) Cotton, F. A. Metal Atom Clusters in Oxide Systems. *Inorg. Chem.* **1964**, *3* (9), 1217–1220. https://doi.org/10.1021/ic50019a003.
(27) Cordier, S.; Molard, Y.; Brylev, K. A.; Mironov, Y. V.; Grasset, F.; Fabre, B.; Naumov, N. G. Advances in the Engineering of Near Infrared Emitting Liquid Crystals and Copolymers, Extended Porous Frameworks, Theranostic Tools and Molecular Junctions Using Tailored Re_6 Cluster Building Blocks. *J. Clust. Sci.* **2015**, *26* (1), 53–81. https://doi.org/10.1007/s10876-014-0734-0.
(28) Kirakci, K.; Shestopalov, M. A.; Lang, K. Recent Developments on Luminescent Octahedral Transition Metal Cluster Complexes towards Biological Applications. *Coord. Chem. Rev.* **2023**, *481*, 215048. https://doi.org/10.1016/j.ccr.2023.215048.
(29) Nguyen, N. T. K.; Lebastard, C.; Wilmet, M.; Dumait, N.; Renaud, A.; Cordier, S.; Ohashi, N.; Uchikoshi, T.; Grasset, F. A Review on Functional Nanoarchitectonics Nanocomposites Based on Octahedral Metal Atom Clusters (Nb_6, Mo_6, Ta_6, W_6, Re_6): Inorganic 0D and 2D Powders and Films. *Sci. Technol. Adv. Mater.* **2022**, *23* (1), 547–578. https://doi.org/10.1080/14686996.2022.2119101.
(30) Molard, Y. Clustomesogens: Liquid Crystalline Hybrid Nanomaterials Containing Functional Metal Nanoclusters. *Acc. Chem. Res.* **2016**, *49* (8), 1514–1523. https://doi.org/10.1021/acs.accounts.6b00236.
(31) Aubert, T.; Ledneva, A. Y.; Grasset, F.; Kimoto, K.; Naumov, N. G.; Molard, Y.; Saito, N.; Haneda, H.; Cordier, S. Synthesis and Characterization of $A_4[Re_6Q_8L_6]@SiO_2$ Red-Emitting Silica Nanoparticles Based on Re_6 Metal Atom Clusters (A = Cs or K, Q = S or Se, and L = OH or CN). *Langmuir* **2010**, *26* (23), 18512–18518. https://doi.org/10.1021/la103784v.
(32) Dierre, B.; Costuas, K.; Dumait, N.; Paofai, S.; Amela-Cortes, M.; Molard, Y.; Grasset, F.; Cho, Y.; Takahashi, K.; Ohashi, N.; Uchikoshi, T.; Cordier, S. Mo_6 Cluster-Based Compounds for Energy Conversion Applications: Comparative Study of Photoluminescence and Cathodoluminescence. *Sci. Technol. Adv. Mater.* **2017**, *18* (1), 458–466. https://doi.org/10.1080/14686996.2017.1338496.
(33) Kepenekian, M.; Molard, Y.; Costuas, K.; Lemoine, P.; Gautier, R.; Girard, S. A.; Fabre, B.; Turban, P.; Cordier, S. Red-NIR Luminescence of Mo_6 Monolayered Assembly Directly Anchored on Au(001). *Mater. Horiz.* **2019**, *6* (9), 1828–1833. https://doi.org/10.1039/C9MH00724E.
(34) Maverick, A. W.; Gray, H. B. Luminescence and Redox Photochemistry of the Molybdenum(II) Cluster $Mo_6Cl_{14}^{2-}$. *J. Am. Chem. Soc.* **1981**, *103* (5), 1298–1300. https://doi.org/10.1021/ja00395a088.
(35) Schäfer, H.; Schnering, H.-G. V.; Tillack, J.; Kuhnen, F.; Wöhrle, H.; Baumann, H. Neue Untersuchungen über die Chloride des Molybdäns. *Z. Für Anorg. Allg. Chem.* **1967**, *353* (5–6), 281–310. https://doi.org/10.1002/zaac.19673530510.
(36) Renaud, A.; Grasset, F.; Dierre, B.; Uchikoshi, T.; Ohashi, N.; Takei, T.; Planchat, A.; Cario, L.; Jobic, S.; Odobel, F.; Cordier, S. Inorganic Molybdenum Clusters as Light-Harvester in All

Inorganic Solar Cells: A Proof of Concept. *ChemistrySelect* **2016**, *1* (10), 2284–2289. https://doi.org/10.1002/slct.201600508.
(37) Akagi, S.; Fujii, S.; Kitamura, N. A Study on the Redox, Spectroscopic, and Photophysical Characteristics of a Series of Octahedral Hexamolybdenum(II) Clusters: $[\{Mo_6X_8\}Y_6]^{2-}$ (X, Y = Cl, Br, or I). *Dalton Trans.* **2018**, *47* (4), 1131–1139. https://doi.org/10.1039/C7DT04485B.
(38) Maverick, A. W.; Najdzionek, J. S.; MacKenzie, D.; Nocera, D. G.; Gray, H. B. Spectroscopic, Electrochemical, and Photochemical Properties of Molybdenum(II) and Tungsten(II) Halide Clusters. *J. Am. Chem. Soc.* **1983**, *105* (7), 1878–1882. https://doi.org/10.1021/ja00345a034.
(39) Costuas, K.; Garreau, A.; Bulou, A.; Fontaine, B.; Cuny, J.; Gautier, R.; Mortier, M.; Molard, Y.; Duvail, J.-L.; Faulques, E.; Cordier, S. Combined Theoretical and Time-Resolved Photoluminescence Investigations of $[Mo_6Br^i_8Br^a_6]^{2-}$ Metal Cluster Units: Evidence of Dual Emission. *Phys. Chem. Chem. Phys.* **2015**, *17* (43), 28574–28585. https://doi.org/10.1039/C5CP03960F.
(40) Frech, P.; Leis, W.; Pachel, F.; Seitz, M.; Meyer, H.-J.; Scheele, M. Time- and Temperature-Resolved Triplet Dynamics in Tungsten Iodide Clusters. *Inorg. Chem.* **2025**, *64* (41), 20584–20595. https://doi.org/10.1021/acs.inorgchem.5c02344.
(41) Molard, Y.; Taupier, G.; Paofai, S.; Cordier, S. Evidencing $((n\text{-}C_4H_9)_4N)_2[W_6I_{14}]$ Red–NIR Emission and Singlet Oxygen Generation by Two Photon Absorption. *Chem. Commun.* **2021**, *57* (33), 4003–4006. https://doi.org/10.1039/D1CC00751C.
(42) Mikhaylov, M. A.; Sokolov, M. N. Molybdenum Iodides – from Obscurity to Bright Luminescence. *Eur. J. Inorg. Chem.* **2019**, *2019* (39–40), 4181–4197. https://doi.org/10.1002/ejic.201900630.
(43) Sheldon, J. C. 621. Chloride Exchange and Bromide Substitution of the Hexachloro-Octa-μ3-Chlorohexamolybdate(II) Ion. *J. Chem. Soc. Resumed* **1960**, No. 0, 3106–3109. https://doi.org/10.1039/JR9600003106.
(44) Sheldon, J. C. 76. Bromo- and Iodo-Molybdenum(II) Compounds. *J. Chem. Soc. Resumed* **1962**, No. 0, 410–415. https://doi.org/10.1039/JR9620000410.
(45) Sheldon, J. C. Polynuclear Complexes of Molybdenum(II). *Nature* **1959**, *184* (4694), 1210–1213. https://doi.org/10.1038/1841210a0.
(46) Hogue, R. D.; McCarley, R. E. Chemistry of Polynuclear Metal Halides. V. Reactions and Characterization of Compounds Containing Tungsten Halide Cluster Species. *Inorg. Chem.* **1970**, *9* (6), 1354–1360. https://doi.org/10.1021/ic50088a012.
(47) Ivanov, A. A.; Haouas, M.; Evtushok, D. V.; Pozmogova, T. N.; Golubeva, T. S.; Molard, Y.; Cordier, S.; Falaise, C.; Cadot, E.; Shestopalov, M. A. Stabilization of Octahedral Metal Halide Clusters by Host-Guest Complexation with γ-Cyclodextrin: Toward Nontoxic Luminescent Compounds. *Inorg. Chem.* **2022**, *61* (36), 14462–14469. https://doi.org/10.1021/acs.inorgchem.2c02468.
(48) Assaf, K. I.; Nau, W. M. The Chaotropic Effect as an Assembly Motif in Chemistry. *Angew. Chem. Int. Ed.* **2018**, *57* (43), 13968–13981. https://doi.org/10.1002/anie.201804597.
(49) Ivanov, A. A.; Falaise, C.; Abramov, P. A.; Shestopalov, M. A.; Kirakci, K.; Lang, K.; Moussawi, M. A.; Sokolov, M. N.; Naumov, N. G.; Floquet, S.; Landy, D.; Haouas, M.; Brylev, K. A.; Mironov, Y. V.; Molard, Y.; Cordier, S.; Cadot, E. Host-Guest Binding Hierarchy within Redox- and Luminescence-Responsive Supramolecular Self-Assembly Based on Chalcogenide Clusters and Gamma-Cyclodextrin. *Chem.- Eur. J.* **2018**, *24* (51), 13467–13478. https://doi.org/10.1002/chem.201802102.
(50) Falaise, C.; Ivanov, A. A.; Molard, Y.; Cortes, M. A.; Shestopalov, M. A.; Haouas, M.; Cadot, E.; Cordier, S. From Supramolecular to Solid State Chemistry: Crystal Engineering of Luminescent Materials by Trapping Molecular Clusters in an Aluminium-Based Host Matrix. *Mater. Horiz.* **2020**, *7* (9), 2399–2406. https://doi.org/10.1039/d0mh00637h.

(51) Mattes, R. Heteropoly and Isopoly Oxometalates. Von M. T. Pope. Springer-Verlag, Berlin 1983. XIII, 180 S., Geb. DM 124.00. *Angew. Chem.* **1984**, *96*, 730–730. https://doi.org/10.1002/ange.19840960939.
(52) Pope, M. T.; Müller, A. Polyoxometalate Chemistry: An Old Field with New Dimensions in Several Disciplines. *Angew. Chem. Int. Ed. Engl.* **1991**, *30* (1), 34–48. https://doi.org/10.1002/anie.199100341.
(53) Hill, C. L. Introduction: Polyoxometalates Multicomponent Molecular Vehicles To Probe Fundamental Issues and Practical Problems. *Chem. Rev.* **1998**, *98* (1), 1–2. https://doi.org/10.1021/cr960395y.
(54) Ammam, M. Polyoxometalates: Formation, Structures, Principal Properties, Main Deposition Methods and Application in Sensing. *J. Mater. Chem. A* **2013**, *1* (21), 6291–6312. https://doi.org/10.1039/C3TA01663C.
(55) Gumerova, N. I.; Rompel, A. Synthesis, Structures and Applications of Electron-Rich Polyoxometalates. *Nat. Rev. Chem.* **2018**, *2* (2), 0112. https://doi.org/10.1038/s41570-018-0112.
(56) Liu, J.-X.; Zhang, X.-B.; Li, Y.-L.; Huang, S.-L.; Yang, G.-Y. Polyoxometalate Functionalized Architectures. *Coord. Chem. Rev.* **2020**, *414*, 213260. https://doi.org/10.1016/j.ccr.2020.213260.
(57) Proust, A.; Thouvenot, R.; Gouzerh, P. Functionalization of Polyoxometalates: Towards Advanced Applications in Catalysis and Materials Science. *Chem. Commun.* **2008**, No. 16, 1837–1852. https://doi.org/10.1039/B715502F.
(58) Minato, T.; Matsumoto, T.; Ogo, S. Homogeneous Catalytic Reduction of Polyoxometalate by Hydrogen Gas with a Hydrogenase Model Complex. *RSC Adv.* **2019**, *9* (34), 19518–19522. https://doi.org/10.1039/C9RA04396A.
(59) Genovese, M.; Lian, K. Polyoxometalate Modified Inorganic-Organic Nanocomposite Materials for Energy Storage Applications: A Review. *Curr. Opin. Solid State Mater. Sci.* **2015**, *19* (2), 126–137. https://doi.org/10.1016/j.cossms.2014.12.002.
(60) Fabre, B.; Falaise, C.; Cadot, E. Polyoxometalates-Functionalized Electrodes for (Photo)Electrocatalytic Applications: Recent Advances and Prospects. *ACS Catal.* **2022**, *12* (19), 12055–12091. https://doi.org/10.1021/acscatal.2c01847.
(61) Toma, F. M.; Sartorel, A.; Iurlo, M.; Carraro, M.; Parisse, P.; Maccato, C.; Rapino, S.; Gonzalez, B. R.; Amenitsch, H.; Da Ros, T.; Casalis, L.; Goldoni, A.; Marcaccio, M.; Scorrano, G.; Scoles, G.; Paolucci, F.; Prato, M.; Bonchio, M. Efficient Water Oxidation at Carbon Nanotube–Polyoxometalate Electrocatalytic Interfaces. *Nat. Chem.* **2010**, *2* (10), 826–831. https://doi.org/10.1038/nchem.761.
(62) Sadakane, M.; Steckhan, E. Electrochemical Properties of Polyoxometalates as Electrocatalysts. *Chem. Rev.* **1998**, *98* (1), 219–238. https://doi.org/10.1021/cr960403a.
(63) Ueda, T. Electrochemistry of Polyoxometalates: From Fundamental Aspects to Applications. *ChemElectroChem* **2018**, *5* (6), 823–838. https://doi.org/10.1002/celc.201701170.
(64) Fatima, A.; Smortsova, Y.; Falaise, C.; Leclerc, N.; Haouas, M.; Cadot, E.; Cordier, S.; Molard, Y.; Pino, T.; Dablemont, C.; Méallet, R.; Steenkeste, K.; Ha-Thi, M.-H. Photoinduced Electron Transfer between a Noble-Metal-Free $[Mo_6I_8Cl_6]^{2-}$ Cluster and Polyoxometalates. *Chem. Commun.* **2023**, *59* (73), 10988–10991. https://doi.org/10.1039/D3CC03334A.
(65) Wu, H. Contribution to the chemistry of phosphomolybdic acids, phosphotungstic acids, and allied substances. *J. Biol. Chem.* **1920**, *43* (1), 189–220. https://doi.org/10.1016/S0021-9258(18)86325-6.
(66) Téazéa, A.; Hervéa, G.; Finke, R. G.; Lyon, D. K. α-, β-, and γ-Dodecatungstosilicic Acids: Isomers and Related Lacunary Compounds. In *Inorganic Syntheses*; John Wiley & Sons, Ltd, 1990; pp 85–96. https://doi.org/10.1002/9780470132586.ch16.

(67) Rocchiccioli-Deltcheff, C.; Fournier, M.; Franck, R.; Thouvenot, R. Vibrational Investigations of Polyoxometalates. 2. Evidence for Anion-Anion Interactions in Molybdenum(VI) and Tungsten(VI) Compounds Related to the Keggin Structure. *Inorg. Chem.* **1983**, *22* (2), 207–216. https://doi.org/10.1021/ic00144a006.
(68) Contant, R.; Klemperer, W. G.; Yaghi, O. Potassium Octadecatungstodiphosphates(V) and Related Lacunary Compounds. In *Inorganic Syntheses*; John Wiley & Sons, Ltd, 1990; pp 104–111. https://doi.org/10.1002/9780470132586.ch18.
(69) Zietlow, T. C.; Hopkins, M. D.; Gray, H. B. Electronic Spectroscopy and Photophysics of d^4 Clusters. *J. Solid State Chem.* **1985**, *57* (1), 112–119. https://doi.org/10.1016/S0022-4596(85)80064-5.
(70) Zietlow, T. C.; Nocera, D. G.; Gray, H. B. Photophysics and Electrochemistry of Hexanuclear Tungsten Halide Clusters. *Inorg. Chem.* **1986**, *25* (9), 1351–1353. https://doi.org/10.1021/ic00229a011.
(71) Papaconstantinou, E. Photochemistry of Polyoxometallates of Molybdenum and Tungsten and/or Vanadium. *Chem. Soc. Rev.* **1989**, *18* (0), 1–31. https://doi.org/10.1039/CS9891800001.
(72) Ivanov, A. A.; Falaise, C.; Shmakova, A. A.; Leclerc, N.; Cordier, S.; Molard, Y.; Mironov, Y. V.; Shestopalov, M. A.; Abramov, P. A.; Sokolov, M. N.; Haouas, M.; Cadot, E. Cyclodextrin-Assisted Hierarchical Aggregation of Dawson-Type Polyoxometalate in the Presence of {Re6Se8} Based Clusters. *Inorg. Chem.* **2020**, *59* (16), 11396–11406. https://doi.org/10.1021/acs.inorgchem.0c01160.
(73) Ivanov, A. A.; Abramov, P. A.; Haouas, M.; Molard, Y.; Cordier, S.; Falaise, C.; Cadot, E.; Shestopalov, M. A. Supramolecular Host-Guest Assemblies of $[M_6Cl_{14}]^{(2-)}$, M = Mo, W, Clusters with Gamma-Cyclodextrin for the Development of CLUSPOMs. *Inorganics* **2023**, *11* (2), 77. https://doi.org/10.3390/inorganics11020077.
(74) Wu, Y.; Shi, R.; Wu, Y.-L.; Holcroft, J. M.; Liu, Z.; Frasconi, M.; Wasielewski, M. R.; Li, H.; Stoddart, J. F. Complexation of Polyoxometalates with Cyclodextrins. *J. Am. Chem. Soc.* **2015**, *137* (12), 4111–4118. https://doi.org/10.1021/ja511713c.
(75) Yao, S.; Falaise, C.; Ivanov, A. A.; Leclerc, N.; Hohenschutz, M.; Haouas, M.; Landy, D.; Shestopalov, M. A.; Bauduin, P.; Cadot, E. Hofmeister Effect in the Keggin-Type Polyoxotungstate Series. *Inorg. Chem. Front.* **2021**, *8* (1), 12–25. https://doi.org/10.1039/D0QI00902D.
(76) Segado-Centellas, M.; Falaise, C.; Leclerc, N.; Priso, G. M.; Haouas, M.; Cadot, E.; Bo, C. Nanoconfinement of Polyoxometalates in Cyclodextrin: Computational Inspections of the Binding Affinity and Experimental Demonstrations of Reactivity Modulation. *Chem. Sci.* **2024**, *15* (38), 15849–15857. https://doi.org/10.1039/D4SC01949K.
(77) Moussawi, M. A.; Leclerc-Laronze, N.; Floquet, S.; Abramov, P. A.; Sokolov, M. N.; Cordier, S.; Ponchel, A.; Monflier, E.; Bricout, H.; Landy, D.; Haouas, M.; Marrot, J.; Cadot, E. Polyoxometalate, Cationic Cluster, and γ-Cyclodextrin: From Primary Interactions to Supramolecular Hybrid Materials. *J. Am. Chem. Soc.* **2017**, *139* (36), 12793–12803. https://doi.org/10.1021/jacs.7b07317.

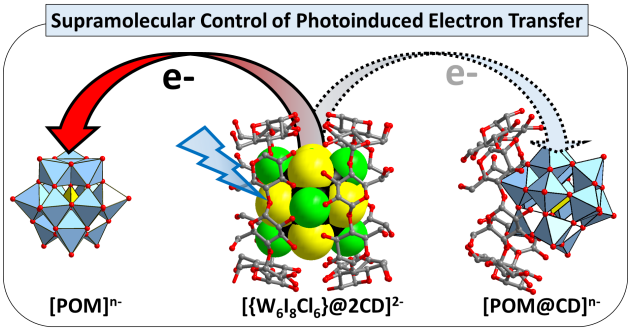

For Table of Contents Only